International Journal of Heat and Mass Transfer 125 (2018) 1003–1016

Contents lists available at ScienceDirect

International Journal of Heat and Mass Transfer

journal homepage: www.elsevier.com/locate/ijhmt

Unsteady analysis of adiabatic film cooling effectiveness behind circular, shaped, and sand-dune–inspired film cooling holes: Measurement using fast-response pressure-sensitive paint

Wenwu Zhou [a,b], Di Peng [a,b], Xin Wen [a,b], Yingzheng Liu [a,b,*], Hui Hu [c]

[a] Key Lab of Education Ministry for Power Machinery and Engineering, School of Mechanical Engineering, Shanghai Jiao Tong University, 800 Dongchuan Road, Shanghai 200240, China
[b] Gas Turbine Research Institute, Shanghai Jiao Tong University, 800 Dongchuan Road, Shanghai 200240, China
[c] Department of Aerospace Engineering, Iowa State University, 2271 Howe Hall, Room 1200, Ames, IA 50011, USA

ARTICLE INFO

Article history:
Received 6 December 2017
Received in revised form 4 March 2018
Accepted 24 April 2018
Available online 5 May 2018

Keywords:
Film cooling
Adiabatic effectiveness
Vortex structure
Pressure sensitive paint

ABSTRACT

The unsteady adiabatic effectiveness behind three types of holes was measured with fast-response pressure-sensitive paint and a high-speed camera, i.e., a circular hole, a shaped hole and the sand-dune–inspired hole. During the experiment, coolant fluid (CO_2) was discharged from a single injection hole at an inclination angle of 35°. The blowing ratio (M) was varied from 0.40 to 1.40. The unsteady behavior of effectiveness was quantified clearly in terms of standard deviations (SDs), spatial correlations, and dynamic mode decomposition. In contrast to the circular hole, the coolant film injected from shaped and Barchan dune-shaped injection compound (BDSIC) holes remained attached to the surface. No separation appeared in any configuration. Especially for the BDSIC concept, significantly greater effectiveness, but a lower SD, was found behind the dune than in the other two configurations. Using two-point spatial correlation, the prominent signatures (i.e., a counter-rotating vortex pair and horseshoe-like vortices) buried in the cross-flow jet were determined, which were responsible for the enhanced SDs in the circular and shaped holes. As for the BDSIC configuration, large-scale coherent structures (i.e., such as circulations, anti–counter-rotating vortex pairs, and strong shear) were identified from the measured effectiveness at blowing ratios (M) of 0.40 and 0.90. Based on dynamic mode decomposition analysis, the corresponding dynamic modes were extracted from the instantaneous effectiveness fields. Although the circular hole featured dominant frequencies (St) of 0.026 and 0.008 at blowing ratios (M) of 0.40 and 0.90, respectively, the BDSIC configuration demonstrated a constant shedding frequency (St) of 0.009. This paper represents the first effort to use fast-response PSP sampling at a high frame rate to quantify the unsteady behavior of adiabatic effectiveness over a flat plate.

1. Introduction

Film cooling, as a state of the art, has been widely implemented in modern gas turbine engines to protect hot-section components from excessive heat. The principle of film cooling is to generate a thin coolant blanket over the protected surface to prevent it from direct exposure to hot gas, hence increasing its working hours [1–5]. A stable and continuous coverage of coolant film is of great importance to ensure the sustainable operation of gas turbine engines. In recent decades, substantial investigations have been undertaken to determine the mean adiabatic cooling effectiveness behind various cooling holes [2,3,5–7]. The mean effectiveness is affected by a series of parameters [1], including the blowing ratio, the momentum flux ratio, the coolant–to–mainstream density ratio, and the coolant hole geometry. Fundamentally, film cooling can be equivalent to a jet in cross-flow (JICF) problem [8–10]. As coolant discharges from the injection holes, it interacts extensively with the mainstream flow. This process gives rise to highly three-dimensional fluid mixing above the wall, leading to complex and unsteady coolant behaviors over the protected surface [10]. As a result, the vital components may be partially or completely exposed to the extremely hot gas due to the unsteady nature of a JICF. A sudden decrease in effectiveness immediately behind the hole may result in local overheating and concentration of thermal stress within the components. Over time, this unstable cooling

* Corresponding author at: Key Lab of Education Ministry for Power Machinery and Engineering, School of Mechanical Engineering, Shanghai Jiao Tong University, 800 Dongchuan Road, Shanghai 200240, China.
E-mail address: yzliu@sjtu.edu.cn (Y. Liu).

https://doi.org/10.1016/j.ijheatmasstransfer.2018.04.126
0017-9310/

Nomenclature

D	diameter of coolant injection hole
D_s	concentration diffusion coefficient
DR	coolant–to–mainstream density ratio, ρ_c/ρ_∞
f	vortex shedding frequency
I	coolant–to–mainstream momentum ratio, $\rho_c U_c^2/\rho_\infty U_\infty^2$
Le	Lewis number, α/D_s
M	blowing ratio or mass flux ratio, $\rho_c U_c/\rho_\infty U_\infty$
MW	molecular weight ratio of coolant to mainstream
$(p_{o_2})_{air}$	partial pressure of oxygen with air as the coolant
$(p_{o_2})_{mix}$	partial pressure of oxygen with non-oxygen gas as the coolant
$R_{\eta'\eta'}$	correlation coefficient
St	Strouhal number, fD/U_∞
T_{aw}	adiabatic wall temperature
T_c	coolant stream temperature
T_∞	temperature of mainstream flow
U_c	coolant stream velocity
U_∞	incoming flow velocity
VR	velocity ratio, U_c/U_∞

Greek symbols

α	thermal diffusion coefficient
θ	injection angle
δ_{99}	boundary layer thickness
δ^{**}	momentum thickness
η	instantaneous film cooling effectiveness
η'	film cooling effectiveness fluctuation
$\overline{\eta}$	ensemble-averaged film cooling effectiveness

Abbreviations

BDSIC	Barchan dune-shaped injection compound
CRV	counter-rotating vortex
DMD	dynamic mode decomposition
PSP	pressure-sensitive paint
SD	standard deviation

behavior would cause fatigue of components and even failure of gas turbine engines. Therefore, a comprehensive understanding of unsteady behaviors of a coolant film over a protected surface is highly desirable.

Pertinent to JICF, several studies have focused on the unsteady behavior of vortex structures under different velocity ratios [5–8]. Karagozian [12], who studied the dynamics of the vorticity at various momentum flux or density ratios, found a jet structure change under different flow conditions. Bidan et al. [11] numerically studied the jet flow-rate modulation effect and reported the domination of shear layer vortices at low blowing ratios. Similar conclusions were reported by Dai et al. [9], who studied the influence of velocity ratios on the flow structures. However, most of those studies focused on the unsteady effect of vortex structures on the flow field, in terms of velocity, vorticity, or other associated turbulence quantities. Very little attention was paid to the unsteady behavior of the coolant film on the test surface, especially the unsteady analysis of adiabatic wall effectiveness. Kalghatgi and Acharya [13] used large eddy simulation to perform dynamic mode decomposition (DMD) of the three-dimensional flow and wall-temperature field and found that the flow structures associated with low and intermediate frequencies make the largest contribution to wall temperature fluctuations. More recently, Khojasteh et al. [14] measured the adiabatic effectiveness behind a circular jet using fast-response pressure-sensitive paint (PSP) and successfully reconstructed the adiabatic wall effectiveness using the most energetic modes of proper orthogonal decomposition. However, the camera in their study was sampling at a low frame rate. The reconstructed effectiveness field would inevitably lose the temporal information, which is highly valuable for the gas turbine community because both the spatial and the temporal variations of adiabatic effectiveness are essentially important.

We performed an unsteady analysis of adiabatic effectiveness behind three representative cooling holes: a circular hole, a shaped hole [7,15], and a Barchan dune-shaped injection compound (BDSIC) configuration [6]. Circular and shaped holes are widely used in gas turbine engines, and their cooling performances are well documented, whereas the BDSIC film cooling concept was recently proposed by Zhou and Hu [6]. Inspired by the unique shape of Barchan dunes commonly seen in deserts that prevents sand particles from being blown away, Zhou and Hu [6] proposed the BDSIC film cooling concept. Their preliminary measurements showed that this design could keep the coolant stream attached to the surface, leading to significantly greater effectiveness over the protected surface. However, spatial and temporal information regarding the adiabatic cooling effectiveness is still lacking.

In this study, while the circular hole was our baseline configuration, the shaped hole and the BDSIC concept were analyzed in detail to compare their spatial and temporal variations of cooling effectiveness over the test surface. Carbon dioxide (CO_2) was used as the coolant fluid and was discharged from a single hole at an inclination angle of 35°. Fast-response PSP measurements were performed in the region where $x/D < 9$ with blowing ratios (M) of 0.4, 0.9, and 1.4. Both the mean and unsteady quantities of adiabatic effectiveness were determined over the whole domain. Two-point spatial correlation was first used to identify the prominent signature above the wall. Dynamic mode decomposition was then performed to extract the dynamic modes associated large-scale structures. This paper represents the first effort to use fast-response PSP sampling at a high frame rate. The coherent structures and dynamic modes identified with spatial correlation and DMD analysis are expected to serve as a benchmark for validation studies in the computational fluid dynamics community.

2. Experimental setup and test models

2.1. Experimental model and test rig

The film cooling experiments were conducted in a low-speed, suction-type wind tunnel in the Department of Mechanical Engineering at Shanghai Jiao Tong University. The tunnel has a 500 × 90 mm^2 optically transparent test section. With honeycombs and multilayer screens installed ahead of the nozzle, the tunnel can supply uniform low-turbulence flow in the test section. Using the hot-wire data measured upstream of coolant hole, the freestream turbulence intensity was measured to be 1.1% with a turbulent integral length scale (i.e., L_x) of 1.5 mm, and the corresponding turbulent time scale is 110 μs.

In this study, all test models were made of a hard-plastic material and manufactured with a rapid prototyping machine. They were constructed layer-by-layer with a resolution of approximately 50 μm. Fig. 1 shows a schematic of the selected film cooling configurations: a circular hole, a shaped hole, and a BDSIC hole. A circular hole with a diameter (D) of 8.0 mm was chosen as the baseline configuration. It has an injection angle of 35° and an entry length of 5D. Fig. 1(b) shows the laidback, fan-shaped hole that

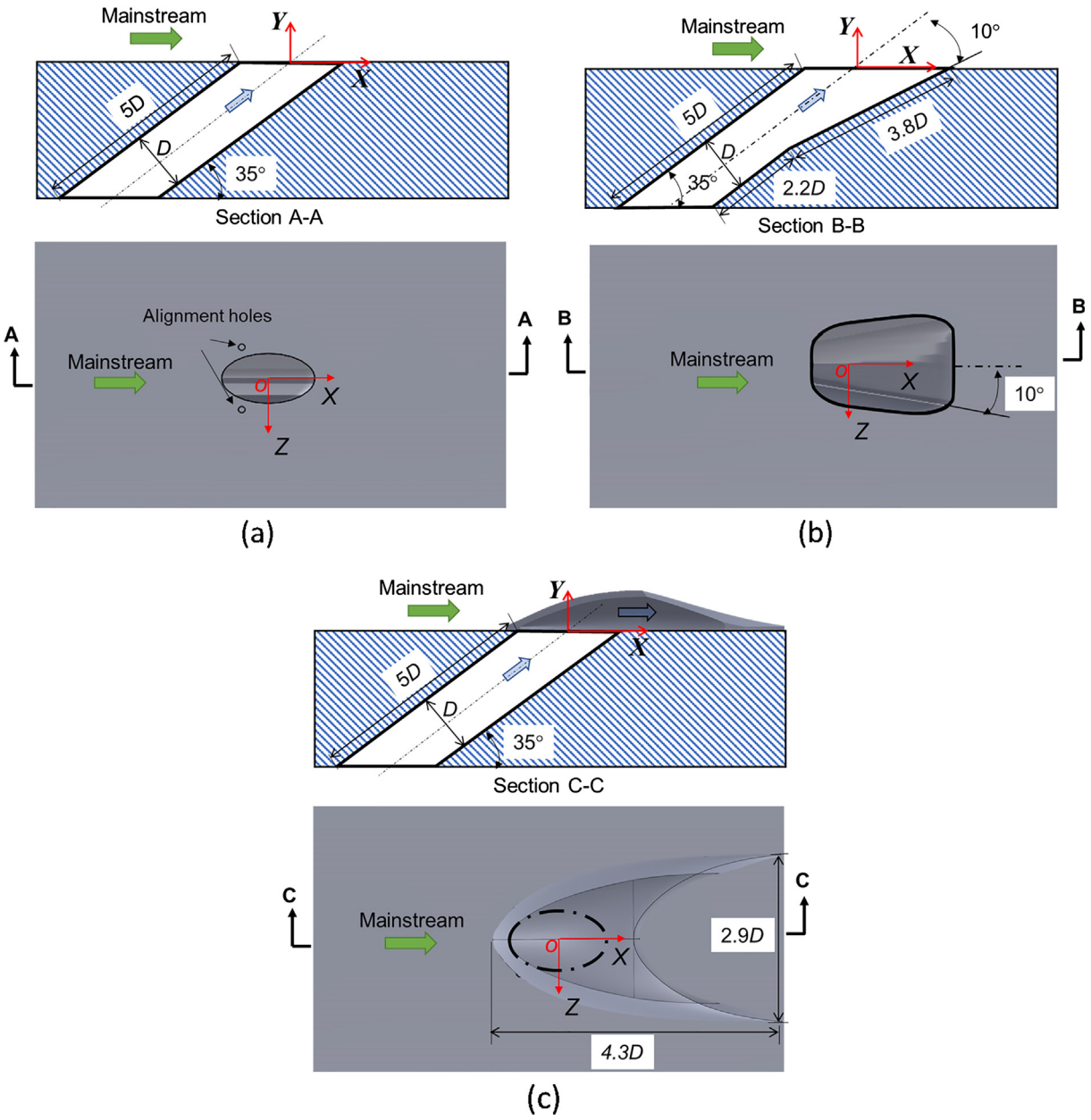

Fig. 1. The schematic of the (a) circular hole, (b) shaped hole, and (c) BDSIC film cooling configuration, where D is the diameter of coolant hole.

opens 10° in the spanwise directions, and 10° laidback toward the surface. It was a reproduction of previously designed hole [7,15]. The BDSIC concept in Fig. 3(b) has the same configuration as that in the literature [6]. The dune shell is 2.9D wide and 4.3D long in the streamwise direction from the dune's leading edge to the horns. The front part of the dune shell is 2.0D long, which could cover the circular hole completely. Therefore, the coolant stream bled from the circular tube would impinge on the dune shell and discharge tangentially into the mainstream. The Barchan-dune shell was affixed to the circular model with 80-μm-thick double-sided glue tape with alignment holes. In this study, while the inlet and outlet of the coolant holes had sharp edges, the internal delivery tube of these holes was carefully polished with 2000-grit sandpaper. The test plate was mounted flush along the bottom wall of the test section. A large-volume plenum chamber (150 × 200 × 180 mm) was sited underneath the test model and sealed with a thin latex rubber gasket to ensure a stable and constant supply of coolant.

Airflow from a wind tunnel was used to simulate the hot gas from the combustor, and an oxygen-free gas (i.e., CO_2 with a density ratio [DR] of 1.5) was supplied to simulate the coolant stream for the PSP measurements. The coolant gas, supplied by a pressurized CO_2 gas cylinder (99.99% purity), passed through a long pipeline and a constant-temperature thermal bath before finally entering the plenum chamber beneath the test plate. The blowing ratios (i.e., mass flux ratios, $M = \rho_c U_c / \rho_\infty U_\infty$) of the test cases were monitored with a flowmeter (Omega, FMA-1610A) and varied from 0.40 to 1.40. The corresponding momentum ratios ($I = \rho_c U_c^2 / \rho_\infty U_\infty^2 = M^2/DR$) were found to range from 0.11 to 1.31, and the velocity ratios ($V_r = U_c/U_\infty$) were varied between 0.3 and 0.9. The mainstream velocity was maintained at a constant speed of 13.6 m/s. The injection holes for all three models were placed at 50D downstream from the leading edge of the test section, and the boundary layer profile was measured immediately upstream of the coolant hole, which was found to be fully developed ($\delta_{99} \approx 1.4D$, momentum thickness $\delta^{**} \approx 0.13D$).

2.2. Adiabatic film cooling effectiveness measurement with PSP technique

Adiabatic film cooling effectiveness, as a nondimensional temperature, is expressed as

$$\eta = \frac{T_\infty - T_{aw}}{T_\infty - T_c} \tag{1}$$

where T_∞ is the temperature of the mainstream flow, T_{aw} is the adiabatic wall temperature under inspection, and T_c is the coolant stream temperature at the hole exit. Apparently, the primary challenge associated with temperature-based methods lies in the measurement of the true adiabatic wall temperature due to the physical reality of heat conduction through the test model.

When the *Lewis number* ($Le = \alpha/D_s$, where α is thermal diffusion and D_s is the concentration diffusion coefficient) for the coolant flow is approximately 1.0, the thermal boundary layer and concentration boundary layer thickness is of the same order, which implies that the differential equations involving heat and mass transfer are analogous [16,17]. Therefore, the PSP measurement is a technique that uses mass transfer to simulate a heat transfer process and has been widely used in recent years. Because PSP measurements are usually conducted under isothermal conditions, the concerns and implications of heat conduction through the test model can be eliminated easily.

In PSP experiments, the measurement of interest is coated with several layers of oxygen-sensitive paint, which consists of luminophores the emit photoluminescence when excited at certain ultraviolet wavelengths. However, the excited molecules may return to the ground state via reduced or radiation-less emission in the presence of diatomic oxygen molecules—the so-called oxygen quenching process—and the intensity of the photoluminescence is inversely proportional to the local oxygen concentration. Consequently, the concentration of oxygen over the interested surface can be calculated based on the recorded light intensity with a calibration curve [14]. Substituting oxygen concentrations for temperatures in Eq. (1), the film cooling effectiveness can be expressed as Eq. (2), as suggested by Charbonnier et al. [18], where *MW* is the molecular weight ratio of the coolant gas to the mainstream gas.

$$\eta = 1 - \frac{1}{[((p_{o_2})_{air}/(p_{o_2})_{mix})_{wall} - 1]MW + 1} \tag{2}$$

The pressures in Eq. (2) can be determined by the recorded intensity of photoluminescence emission, which is inversely proportional to the partial pressure of oxygen. The mathematic function between the normalized intensity and the partial pressure can be obtained with a dedicated PSP calibration procedure. Further technical details about the PSP technique and calibration procedure can be found in the literature [19,20].

Fig. 2 shows the experimental setup for the PSP measurements. To resolve the dynamic of adiabatic effectiveness fluctuations, a fast-response polymer-ceramic PSP (PtTFPP as the luminophore) was applied on the test model, which was prepared in-house and the resonance tube calibration showed a dynamic response of up to 6 kHz (response time ~160 μs) [21,22]. The paint formulation was initially developed by Scroggin [23] et al. and then further improved by Gregory et al. [24]. During the experiment, a high-power ultraviolet LED (LM2X-DM, ISSI) with a wavelength of 390 nm was used as the excitation source for the fast-response PSP measurements. Meanwhile, a high-speed complementary metal oxide semiconductor camera (PCO, HS4) was used to record the photoluminescence light emission at a sampling rate of 500 Hz. A 650 ± 50 nm bandpass filter mounted ahead of the camera was used to filter out background noise from the ambient environment.

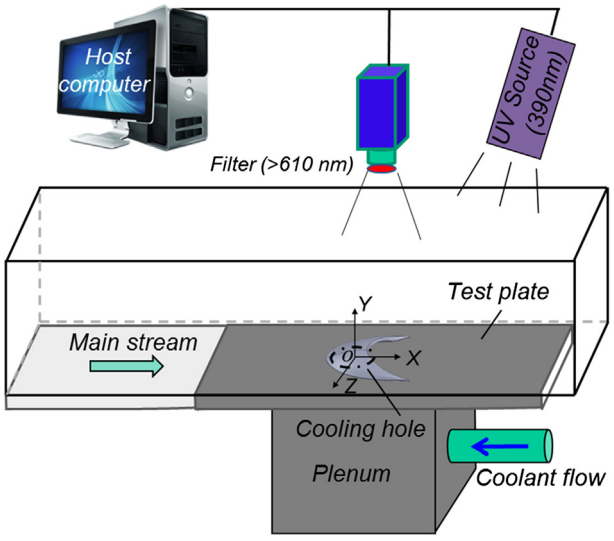

Fig. 2. Experimental setup used for the PSP measurements.

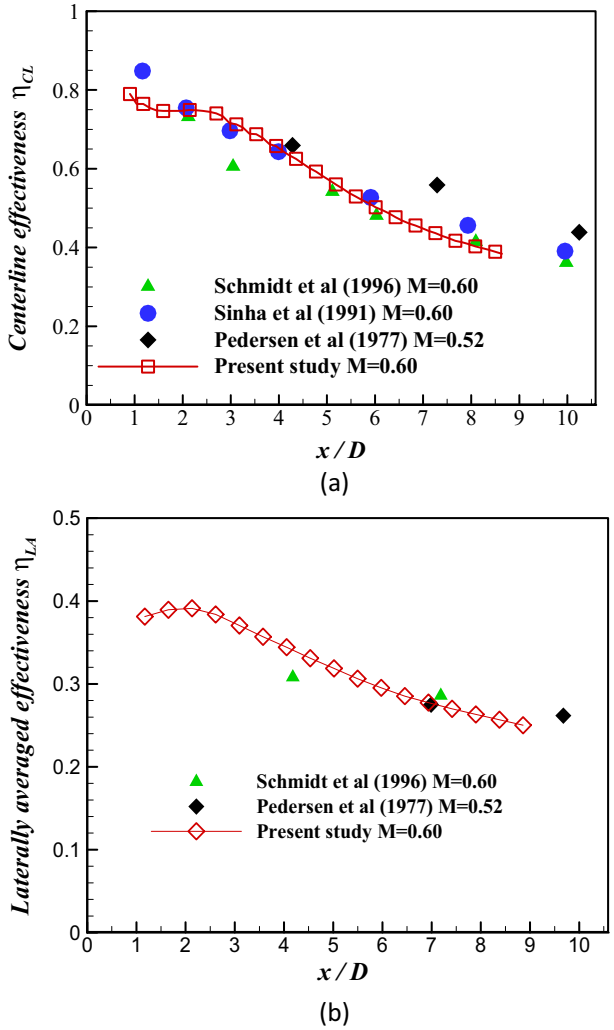

Fig. 3. Comparison of the measured film cooling effectiveness of the present study with those of previous results at $M = 0.60$, $DR = 1.5$.

The experimental study was conducted in isothermal conditions with a constant environmental temperature of 22 ± 0.5 °C.

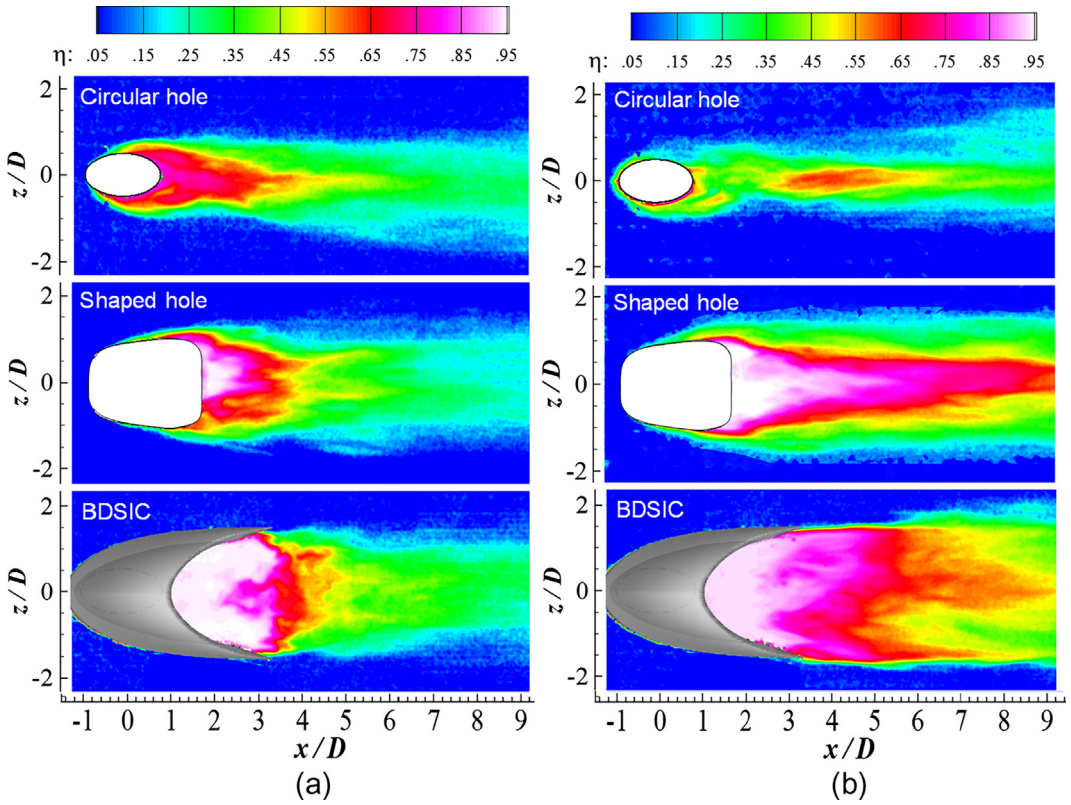

Fig. 4. Typical instantaneous film cooling effectiveness results at blowing ratios of $M = 0.40$ and $M = 0.90$.

In the present study, a spatially averaged procedure with interrogation windows of 9 × 9 pixels and a 50% overlap rate was performed for PSP image processing to minimize the uncertainty of the measurements. The images were recorded at 0.06 mm per pixel, resulting in a spatial resolution of 0.03*D* for the PSP measurement results. Following up on the work of Johnson and Hu [19], the measurement uncertainty was estimated to be within 5% near the hole (i.e., most region $\eta \geqslant 0.5$), which was closely related to the PSP calibration, the quality of the acquired images, and the flow conditions of the mainstream and coolant streams.

3. Measurement results and discussions

3.1. Verification of measured adiabatic effectiveness by using fast-response PSP

A comparative study was first performed to validate the reliability of the fast-response PSP technique. Fig. 3 shows the comparison of the measured film cooling effectiveness with the PSP technique against those of the previous results with similar test conditions (i.e., same blowing and density ratios but different hole entry length). It should be noted that the centerline effectiveness profiles refer to the results measured along the centerline of the injection hole, whereas the laterally-averaged effectiveness values were determined by averaging the effectiveness along the spanwise direction within the region of $-1.5D \leq Z/D \leq 1.5D$. As shown in Fig. 3, both the centerline and laterally-averaged effectiveness profiles were found to be consistent with the archived temperature-based results [25–27] in the measurement region ($1.0 \leq x/D \leq 9.0$). Some discrepancies were detected between the present study and Pedersen et al. [27]'s results downstream, which is believed to be caused by the differences in blowing ratio and incoming boundary layer thickness. Note that the spatial resolution in this study was much higher than those in previous studies. Therefore, based on the preceding discussion, the fast-response PSP technique is believed to be reliable and accurate.

3.2. Instantaneous film cooling effectiveness results

Fig. 4 shows the instantaneous effectiveness distributions behind the three representative film cooling holes at various blowing ratios. Apparently, the coolant flows from the injection holes were found to interact severely with the mainstream flow, leading to highly unstable film distributions over the test surface. At a relatively low blowing ratio (M) of 0.40, the coolant films from the selected holes remained attached to the flat surface, as indicated by the high effectiveness values. Although a similar phenomenon was observed for the shaped and BDSIC holes at a blowing ratio (M) of 0.90, the coolant stream from the circular hole was found to initially separate from the surface near the hole and then reattached further downstream. Similar conclusions were also reported by other researchers [1,6,28].

3.3. Ensemble-averaged effectiveness distributions and statistical quantities

During the experiment, a snapshot dependency study (i.e., with instantaneous effectiveness of 5000, 10,000, 15,000, and 20,000) was conducted firstly to determine the minimum snapshot requirement for results convergence. It was found that the mean effectiveness and statistical quantities would reach a steady value as the number of instantaneous results became greater than 15,000. Therefore, the ensemble-averaged effectiveness results were obtained from a sequence of 15,000 instantaneous PSP measurement results. Fig. 5 shows the measured mean cooling effectiveness and standard deviations (SDs) for the circular hole at blowing ratios (M) of 0.40, 0.90, and 1.40. It shows clearly that the coolant stream injected from the circular hole spread widely over the surface at a blowing ratio (M) of 0.40, indicating good

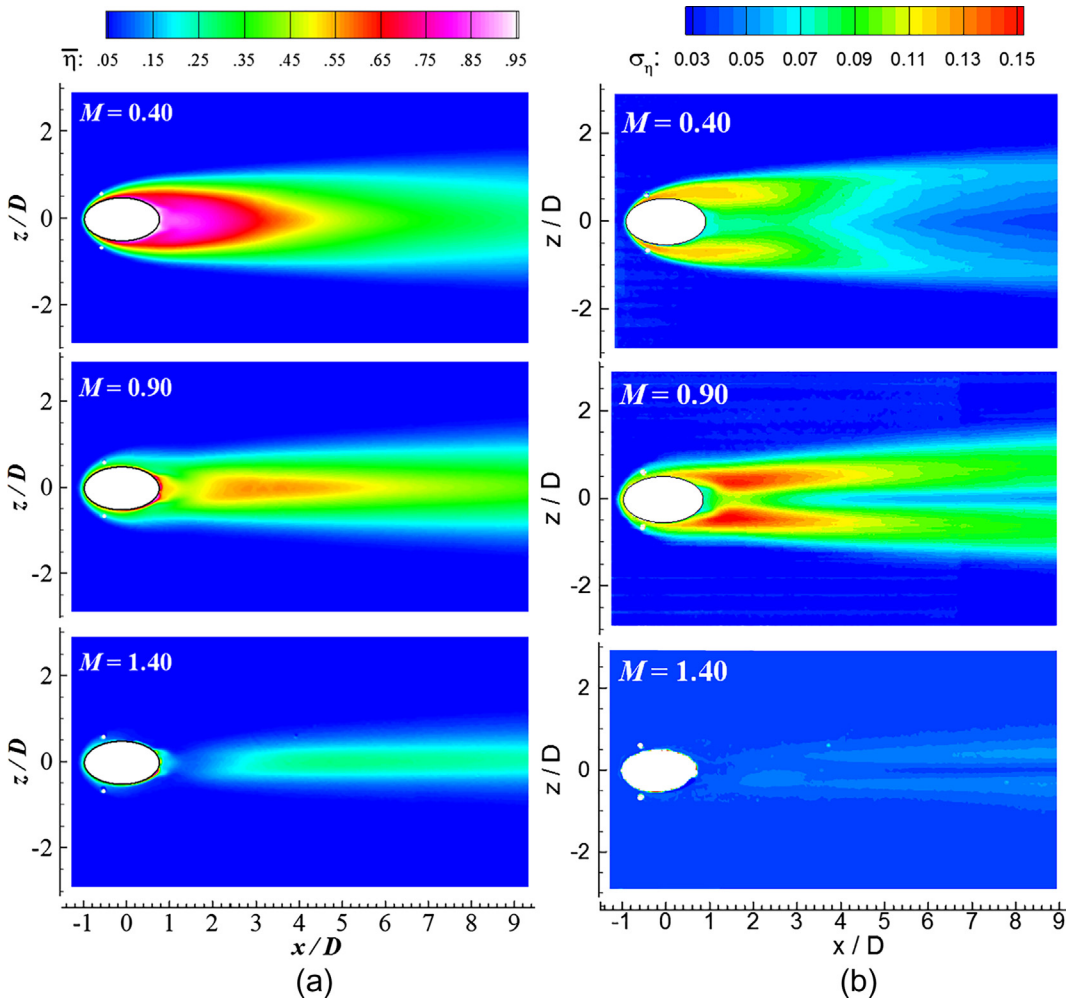

Fig. 5. Measured (a) ensemble-averaged effectiveness and (b) SD distributions for the circular hole case (i.e., baseline) at various blowing ratios.

attachment of the coolant film over the surface of interest. The regions with high effectiveness are shown in white and red[1], and those with lesser effectiveness are shown in blue. At a blowing ratio (M) of 0.40, the red footprint was found to reach approximately 5D downstream but disappeared suddenly due to the insufficient momentum and limited volume of coolant gas at this low blowing ratio. The corresponding SD was found to be completely different from the effectiveness distribution. In contrast to the effectiveness, the SD map exhibited a lower value in the center region, but much higher values along the coolant boundary. As expected, the coolant fluctuations in the center region were much lower than those at the borders, where the coolant interacted intensively with the adjacent mainstream. Therefore, the center region had high cooling effectiveness with less-effective fluctuations. Two strips with relatively high fluctuations were observed at the lateral edges of the circular hole, starting from around the leading edge to approximately 2D downstream. These were believed to be caused by the highly unsteady shear layer vortices as the jet interacts with the mainstream flow [8,13]. As the blowing ratio (M) increased to 0.90, the region with high effectiveness became narrower. The coolant jet was found to separate from the test plate immediately after flow injection, but it reattached approximately 2.5D downstream, which was consistent with the measured PIV results reported by Zhou and Hu [6]. As for the corresponding SD, two strips with significantly high fluctuations were found to spread laterally behind the coolant hole, which is related to the unsteady behaviors associated with jet separation and reattachment. Further increasing the blowing ratio (M) to 1.40, the jet stream completely separated from the surface and penetrated the cross-flow, leading to a poor effectiveness distribution over the surface. As expected, once the coolant jet left the surface, less fluctuation was noticed on the wall surface.

Fig. 6 shows the measured ensemble-averaged effectiveness and SDs for the shaped hole at various blowing ratios. The film cooling effectiveness values for the shaped hole appear to be much higher than those for the circular hole, especially at relatively high blowing ratios. A similar conclusion has also been reached by other researchers [1–3,7,15,28]. Due to jet diffusion along the lateral and laidback directions, a high-momentum jet would stay remain on the surface rather than separating and penetrating the cross-flow. As shown clearly in Fig. 6, the footprints of measured effectiveness became longer and wider as the blowing ratio (M) increased from 0.40 to 1.40. As for the corresponding SDs, the case with a blowing ratio (M) of 0.40 showed a high-fluctuation region at the exit of the shaped hole, whereas the cases with blowing ratios (M) of 0.90 and 1.40 exhibited an almost pure clean region (i.e., very low fluctuation) at the exit region but greatly intensified fluctuations by the sides of the shaped holes. Because the momentum of the coolant jet was relatively weak at a blowing ratio (M) of

[1] For interpretation of color in Fig. 5, the reader is referred to the web version of this article.

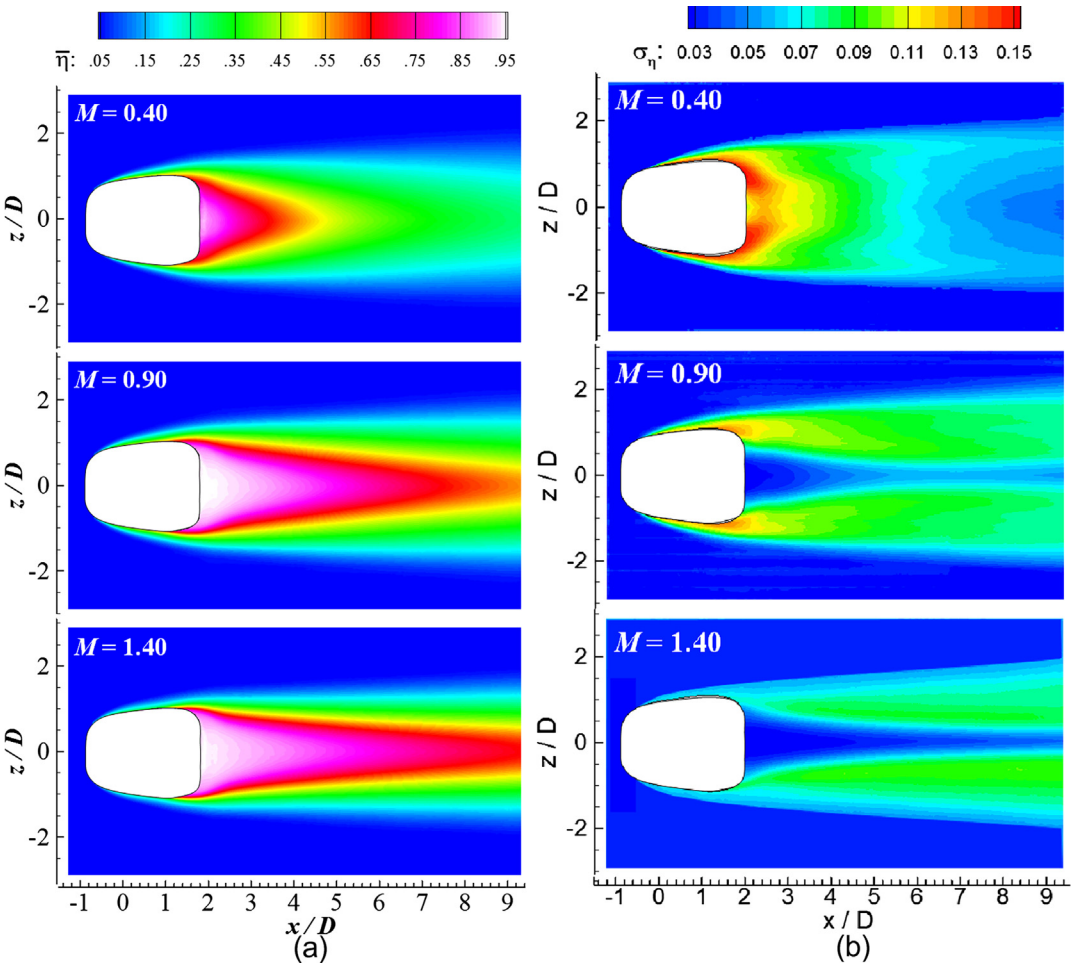

Fig. 6. Measured (a) ensemble-averaged effectiveness and (b) SD distributions for the shaped hole case at various blowing ratios.

0.40, it fluctuated greatly after leaving the hole, leading to greatly enhanced fluctuations near the exit. However, as the M increased to 0.90 and 1.40, the jet momentum was sufficiently high to provide stable film coverage over the center region. Note that, the long ribbons (i.e., regions with augmented fluctuations at approximately z/D = ±1) originating from the sides of the cooling hole were believed to be caused by the unsteady coolant shedding as it interacted with the cross-flow.

Fig. 7 shows the measured mean effectiveness and SDs for the BDSIC configuration at various blowing ratios. Compared with the circular and shaped holes, the effectiveness distributions for the BDSIC configuration were found to have a wider (i.e., spanning from approximately $-2.5D$ to $2.5D$ in the z-direction) and more uniform spread. Due to the BDSIC's special design, the coolant stream impinged on the inner surface of the dune shell and then discharged tangentially into the cross-flow [6]. This process greatly suppressed the takeoff behavior of the jet flow and thus significantly improved the film cooling performance. In addition, the magnitudes of the measured SD, except for the regions along the axis of the dune horns, were found to be much smaller than for the circular and shaped holes at blowing ratios (M) of 0.90 and 1.40. The enhanced SDs along the horn axis were believed to be caused by the three-dimensional anti-CRV and strong shear flow [6]. At a blowing ratio (M) of 0.40, the highest effectiveness and SD regions (i.e., white color) were found to form a V-shape. Because of the strong circulation along the dune horns, the coolant gas from the dune shell tended to flow along the lateral edges of the dune, resulting in relatively low effectiveness in the center.

3.4. Schematic of vortex structures behind circular hole and BDSIC configuration

Revealing the dominant flow structures pertinent to the inclined JICF would deepen understanding of the cause-and-effect modulation of the spatial-temporal features of adiabatic effectiveness [11,13,29]. Before introducing the dynamic information on adiabatic effectiveness, a schematic illustration of the flow structures behind (a) a circular hole and (b) the BDSIC configuration is shown in Fig. 8. Note that, Fig. 8(a) is reprinted from Kalghatgi and Acharya [13], and Fig. 8(b) is reprinted from and Zhou and Hu [6,30]. These experiments shared similar configurations and incoming flow conditions.

For the circular hole, Kalghatgi and Acharya [13] and Sakai [29] used large eddy simulation for numerical investigation of the thermal and hydrodynamic flow field of a round jet. Based on DMD analysis, Kalghatgi and Acharya [13] convincingly demonstrated the dynamics of CRV and horseshoe vortices in the vicinity of a coolant hole. A straightforward view of the vortex structures is exhibited clearly in Fig. 8(a), including the horseshoe vortex, a large-scale CRV pair, and spiral structures. According to the schematic figure, the CRV pair and spiral structures were initially formed at the trailing edge and lateral edge of the hole, respectively, and then merged approximately $1D$ downstream. Nikolaos [31] reported similar coherent flow structures behind the shaped hole. The existence of the CRV pair and horseshoe-like vortices were captured clearly in the coolant jet using large eddy simulation. Due to the lift induced from the CRV pair, these vortices were observed to expand and lift-off

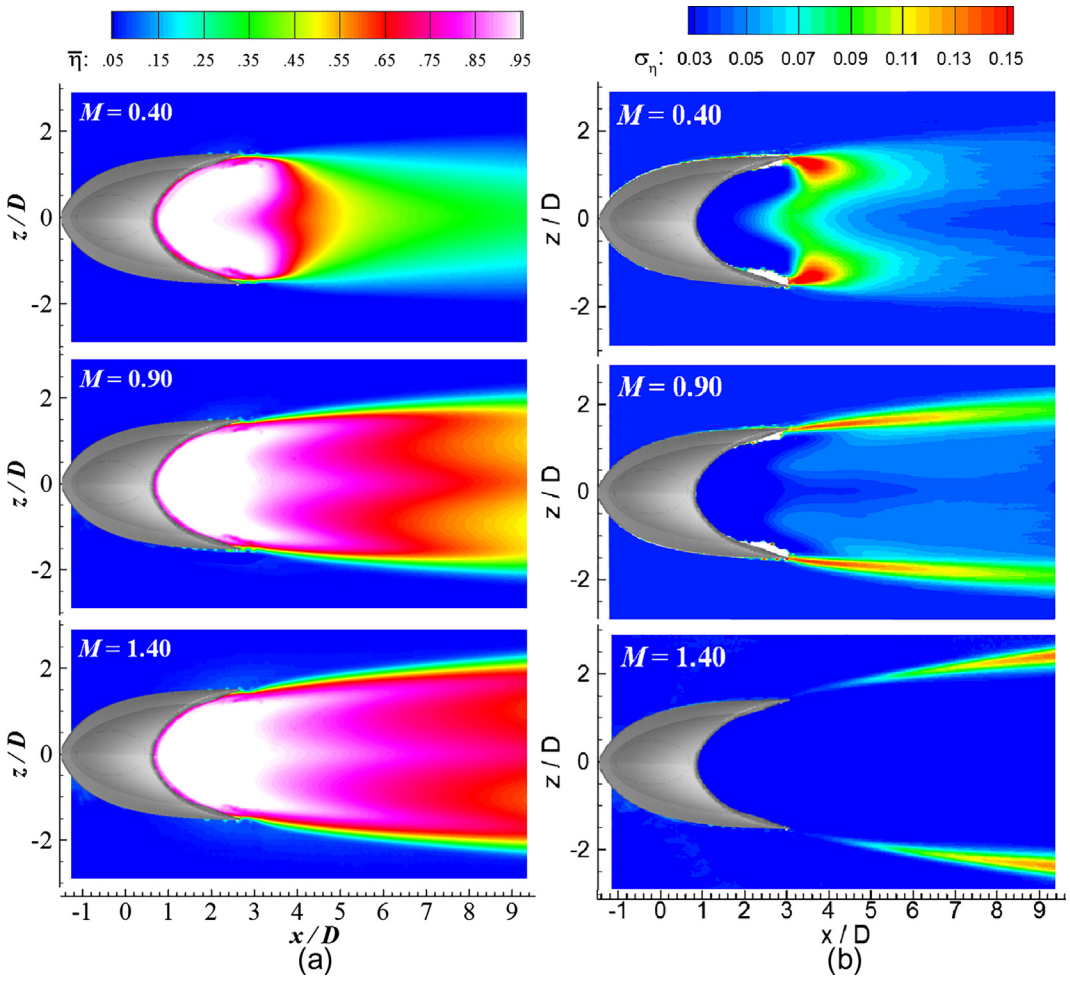

Fig. 7. Measured (a) ensemble-averaged effectiveness and (b) SD distributions for the BDSIC configuration at various blowing ratios.

gradually as they convected downstream. In addition to the circular and shaped holes, Fig. 8(b) vividly illustrates the unique flow features associated with the BDSIC design for improved film cooling effectiveness. It features a tangential jet flow and a pair of large-scale anti-CRV pairs behind the dune shell. The high-speed coolant discharged from the delivery tube impinged on the inner surface of the dune and then emanated tangentially into the cross-flow. Meanwhile, the dominant anti-CRV pair, rotating opposite to the CRV, induced strong downwash flows that spread out the coolant stream laterally. Consequently, the effectiveness behind BDSIC was reported to be much higher than the baseline configuration [6]. When the blowing ratio was relatively small (such as $M = 0.40$), another pair of vortices showed up horizontally in the *X-Z* plane due to the continuing suction along the dune horns [30].

3.5. Two-point spatial correlations

To uncover the coherent structures from the instantaneous effectiveness fields, a zero-time-delay spatial correlation was used to analyze the datasets at reference point (x_0, y_0),

$$R_{\eta'\eta'}((x_0,y_0),(x,y)) = \frac{\overline{\eta'(x_0,y_0)\cdot\eta'(x,y)}}{\sqrt{\overline{\eta'(x_0,y_0)^2}}\cdot\sqrt{\overline{\eta'(x,y)^2}}}, \quad (3)$$

where $R_{\eta'\eta'}((x_0,y_0),(x,y))$ is the correlation coefficient and $\eta'(x_0,y_0)$ is the instantaneous effectiveness fluctuation at the reference point (x_0, y_0). In this study, each correlation coefficient was the time-averaged value of 15,000 instantaneous snapshots. Weak spatial correlations, such as values below $R_{\eta'\eta'} = 0.3$, were filtered out and set to zero to better demonstrate the coherent signatures. Figs. 9–11 show the spatial correlation contours for the circular, shaped, and BDSIC holes at blowing ratios (M) of 0.40 and 0.90. Because very similar results were obtained at a blowing ratio (M) of 1.40, only the correlation maps at $M = 0.90$ are shown here for conciseness.

In general, five reference points were selected to compute the spatial correlations in the circular hole configuration and are shown in Fig. 9. Three were placed around the edge of the hole because most of the coherent structures were initiated from the hole edge. Based on the SD maps shown in Fig. 5, the other two were set 3*D* downstream to avoid potential interference from horseshoe vortices. As expected for $M = 0.40$ in Fig. 9(a), the coherent signatures at P_1 and P_2 were found to be symmetric, originating from the hole's lateral edge and extending to approximately 2.5*D* downstream. These structures were very similar to the SD contours shown in Fig. 5, which were caused by horseshoe vortices as indicated in Fig. 8(a). This also indicates the large contributions of horseshoe vortices on the effectiveness fluctuations at $M = 0.40$. In addition, strong correlations were obtained at locations P_4 and P_5, starting from the cooling hole to all the way across the surface of interest. Careful examination of the correlation contour showed that the signatures initiated separately from both the trailing and lateral edges of the coolant hole and merged into a large coherent structure. A similar phenomenon was also reported by Kalghatgi and Acharya [13], who found CRV pairs and spiral structures gen-

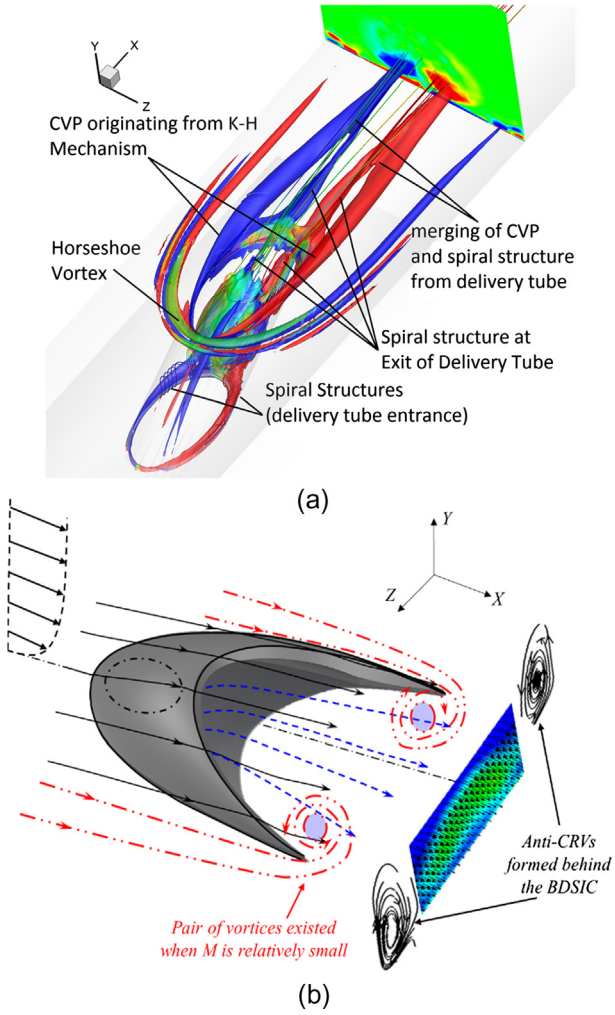

Fig. 8. Schematic illustration of flow structures behind (a) circular hole at $M = 1.0$, $DR = 2.0$ (i.e., reproduced from Kalghatgi and Acharya [13]) and (b) BDSIC cooling concept, $M = 0.9$, $DR = 1.5$ (i.e., reproduced from Zhou and Hu [6,29]).

erated at the trailing and lateral edges of the hole, respectively, which then converged approximately 1*D* downstream. Therefore, the coherent patterns at P_4 and P_5 should be the contributions of both CRV pairs and lateral spiral vortices on film cooling effectiveness over a flat plate. The P_3 presented at the very bottom of Fig. 9 (a) exhibited a high coefficient near the hole, which then gradually decreased along the streamwise direction. This is very similar to the time-averaged effectiveness result, as shown in Fig. 5. Since the coolant was well attached at $M = 0.40$, the structures near the hole buried in JICF remained on the surface, leading to significantly strong contributions on the spatial correlation. Therefore, the correlated area at P_3 is the result of associated large-scale structures.

When the blowing ratio (M) was increased to 0.90, quite similar signatures were observed at P_1 and P_2. As for the structures at P_4 and P_5, it was caused mainly by the CRV pair since no contribution was observed from the lateral shear layer vortices, unlike the aforementioned $M = 0.40$. At $M = 0.90$, the coolant jet was confirmed to partially separate from the test model (i.e., Fig. 5), leading to wider diffusion in the lateral direction. This also explains why the orientation of the coherent signatures at P_4 and P_5 pointed slightly outward. Due to the separation of the coolant jet, the associated JICF structures had a limited effect on the wall coherent signature. Especially near the hole, significantly weak contributions were observed at P_3, where it was a dead zone that did not correlate with other locations.

Fig. 10 shows the two-point spatial correlations for the shaped hole at blowing ratios (M) of 0.40 and 0.90. The general patterns appear to be quite similar for both configurations. The spatial correlations around the hole edges (i.e., P_1 and P_2) exhibit the local contributions of horseshoe-like vortices on the coherent pattern of effectiveness. Meanwhile, the coherent areas at P_4 and P_5 demonstrate the relative effects of the CRV pairs in the shaped hole [31]. Note that the coherent areas at P_4 and P_5 for the test case with $M = 0.90$ were slightly larger than that of the $M = 0.40$ case, indicating an increase in the strength of CRV with the increase in momentum, which was consistent with the measurement results of Sakai et al. [29]. However, reference point P_3 was found to have almost no correlation to any other points, quite unlike the results shown in Fig. 9. One plausible explanation is that the discharged coolant stream from the shaped hole turned into a thin film that was bound strongly by the wall surface and independent from the vicinity coolant; therefore, the coherence of the wall-bounded jet decreased greatly.

Regarding the spatial contours of the BDSIC hole, it is shown in Fig. 11. Ten reference points were selected to demonstrate the coherent signatures in the adiabatic effectiveness field of the BDSIC hole. Three points were placed in the bay of the dune, two at $X/D = 3.5$ immediately behind the dune horns, and the other five at 6*D* downstream locations. More information can be found in the table shown in Fig. 11 (a). Recall that, the vortex structures behind the BDSIC are typically featured by a tangential jet flow and a pair of large-scale anti-CRV pairs (i.e., in the *Y-Z* plane) that originated from the horns of the dune. As shown in Fig. 8(b), when the blowing ratio is relatively small, such as 0.40, an additional pair of vortices appeared in the bay of the BDSIC (i.e., in the *X-Z* plane). Namely, the coherent structures at P_1 and P_3, with a long and narrow pattern formed along the lateral edge of the horns, were the contributions of large-scale vortices in the *X-Z* plane. As for the reference points at P_4 and P_5, these locations not only experienced intensive velocity shear, but also underwent strong induced flow since the anti-CRV pairs were generated here. Therefore, the correlated regions at P_4 and P_5 were the resultant effect of both shear and anti-CRV pairs, which contributed most to the high SDs, as shown in Fig. 7. At $M = 0.40$, the relatively low momentum of the coolant jet caused the mainstream flow to bend slightly inward and interact intensively with the coolant flow. This process was demonstrated clearly by the large coherent structure at P_8. The patterns generated at P_6 and P_{10} represent the regions affected by the anti-CRV pairs in the mainstream flow. Based on the preceding discussion, we can roughly outline the interfaces between the coolant and mainstream flow, which are shown in dash-dot lines in Fig. 11 (b); this is also the trajectory of the anti-CRV pairs. In general, the complex coherent structures directly confirm the highly three-dimensional flow behavior behind the BDSIC at a blowing ratio (M) of 0.40, which is consistent with the measured effectiveness fluctuations in Fig. 7(b).

Increasing the blowing ratio to $M = 0.90$, the jet was sufficiently strong to overcome the continuous suction [30] behind the dune. It was found to bleed out directly into the cross-flow rather than circulate in the bay of the dune, which was confirmed quantitatively by the crescent-shaped correlation at P_2. In contrast to the inconsistent behaviors at $M = 0.40$, the coolant in the bay at $M = 0.90$ exhibited a coordinated action, resulting in a large area at P_2. It is worthy of mention that significant shear was found within the coolant and mainstream flow, as illustrated vividly by the reference points (i.e., P_4 and P_5, P_6 and P_{10}, and P_7 and P_9). Whereas the regions at P_4, P_5, P_7, and P_9 outlined the coolant stream behind the dune shell, the areas at P_6 and P_{10} depicted the coherent structures in the mainstream flow. Two dash-dot lines are plotted in Fig. 11(b) to shows the approximate trajectory of the anti-CRV pairs behind the dune. Its location is consistent with the measured

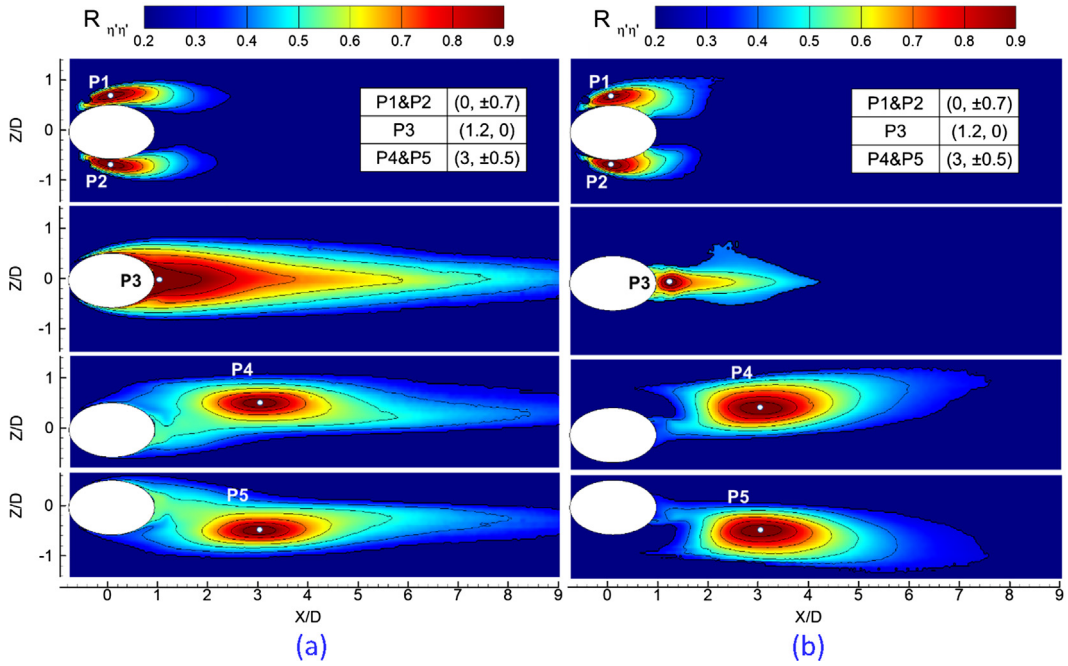

Fig. 9. Two-point spatial correlation for circular hole at blowing ratio of (a) $M = 0.4$ and (b) $M = 0.9$.

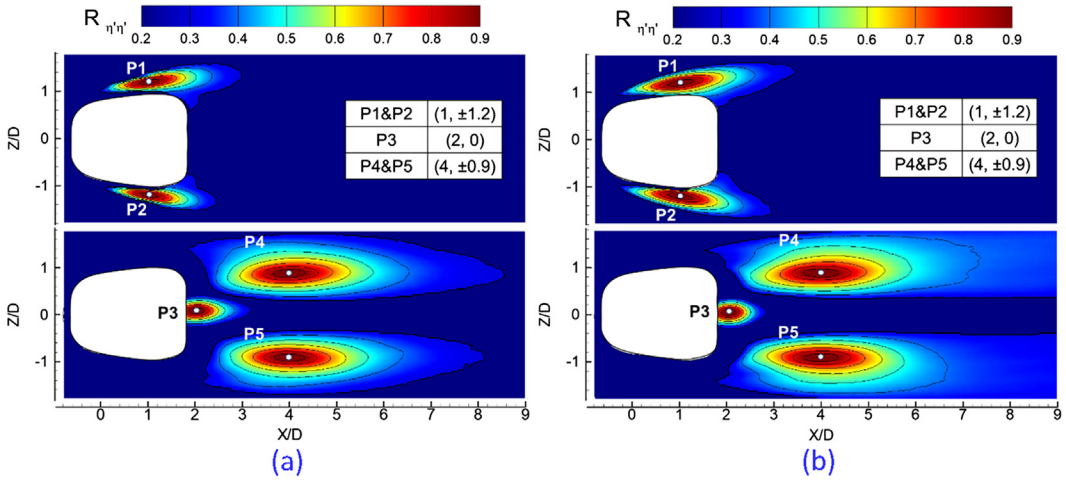

Fig. 10. Two-point spatial correlation for the shaped hole at blowing ratios of (a) $M = 0.4$ and (b) $M = 0.9$.

stereoscopic PIV results presented by Zhou and Hu [6]. As expected, the effectiveness fluctuations on the wall along the axis of the dune were significantly higher than those at the rest of the locations due to the significant shear and three-dimensional anti-CRV pair effect.

In general, the two-point spatial correlation clearly demonstrates the contributions of large-scale vortices on film cooling effectiveness. While the horseshoe vortices and CRV vortex pairs were confirmed to play major roles in the coherent structure of effectiveness for the circular and shaped holes, the high shear and anti-CRV pairs were believed to make the greatest contributions in the BDSIC configuration.

3.6. DMD analysis

DMD analysis is a quantitative method proposed and modified by Schmid [32,33] to extract dynamic information from unsteady flows. Unlike the proper orthogonal decomposition based on energy percentage, the DMD method extracts coherent structures according to their contributions to the flow dynamics. Therefore, the DMD approach is a useful tool in quantifying the flow dynamic by supplying a series of energetic spatial modes by means of frequency content.

A time-sequence dataset is arranged into a major matrix H_1^N,

$$\mathrm{H}_1^N = \{\eta_1, \eta_2, \cdots, \eta_N\} \tag{4}$$

where η_i is a representative instantaneous effectiveness at time t_i. If there exists a linear matrix A that transforms η_i into η_{i+1}, we can obtain the following expression:

$$\mathrm{H}_1^N = \{\eta_1, A\eta_1, \cdots, A^{N-1}\eta_1\}. \tag{5}$$

Therefore, the dynamic characteristics are described by matrix A, and the effectiveness field can be provided by the following $\eta(x, t)$:

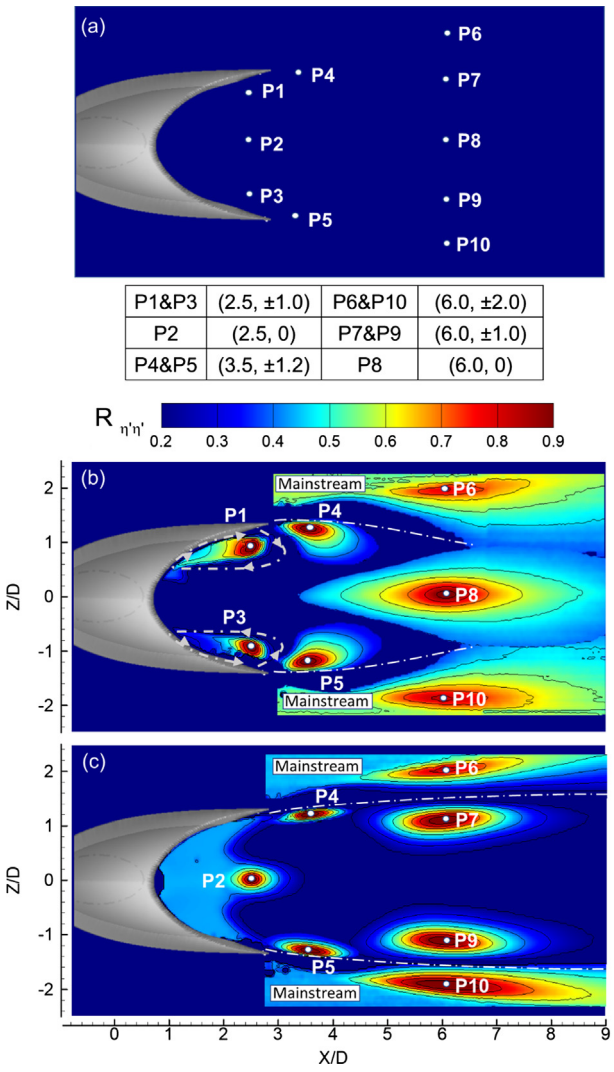

Fig. 11. Two-point spatial correlation for the BDSIC hole at blowing ratios of (b) M = 0.4 and (c) M = 0.9, where (a) shows the reference points and corresponding locations.

$$\eta(x,t) = \sum_{n=1}^{N} b_n \exp(\mu_n t)\Psi_n(x), \tag{6}$$

where b_n is the corresponding amplitude and μ_n is the frequency. As for the DMD mode, Ψ_n can be expressed as

$$\Psi_n(x) = \mathrm{H}_1^{N-1} X_n \tag{7}$$

where X_n is the eigenvector of matrix A; Ψ_n represents the system matrix in DMD analysis. Readers who wish for more detailed information associated with the DMD analysis are referred to Schmid [32,33].

In this study, to uncover the dynamic information of the effectiveness field, DMD analysis was applied to extract the dominant mode from the acquired large datasets. Figs. 12 and 13 show the results of DMD analysis for the circular hole and BDSIC configurations at blowing ratios (M) of 0.40 and 0.90, respectively. Since no dominant frequency was identified for the shaped hole, only the results for circular and BDSIC holes are shown here for conciseness.

The spectral power density for the circular configuration at M = 0.40 is shown on the left-side of Fig. 12(a), which consists of a wide range of frequencies. The neutral mode with 0 Hz at the origin location represents the mean effectiveness, non-oscillating mode. The first peak is the most energetic oscillating mode, which has a frequency of 45 Hz. Its corresponding Strouhal number (fD/U_∞) is St = 0.026, where f is the shedding frequency, D is the diameter of the coolant hole, and U_∞ is the mainstream velocity. However, the energy levels of the peak and its harmonics (i.e., St = 0.026, 0.052, 0.080...) are considerably lower in comparing to the total energy content. Their corresponding dynamic modes (i.e., imaginary part only) are displayed in Fig. 12(b), which clearly shows that the coherent mode structures for M = 0.40 became smaller as the Strouhal number increased from 0.026 to 0.052, indicating a dynamic vortex breakup and dissipated process within the JICF.

The right side of Fig. 12 displays the corresponding DMD analysis results for the case with a blowing ratio (M) of 0.90. As expected, due to the separation of the coolant jet, the energy spectra for the M = 0.90 case was found to scatter broadly, and no obvious dominant frequency was identified, except for a weak peak at 13 Hz (i.e., corresponding St = 0.008). This frequency is probably associated with the unsteady jet reattachment process (i.e., region denoted by dash-lines), which was confirmed qualitatively by the shape of dynamic mode. The general pattern of the dynamic mode is very similar to the SD distribution shown in Fig. 5(b).

Fig. 13 shows the DMD analysis for the BDSIC at blowing ratios (M) of 0.40 (left) and 0.90 (right). Fig. 13(a) clearly shows that two oscillating frequencies (i.e., 15 and 57 Hz; corresponding to St = 0.009 and 0.034, respectively) are recognized from the energy spectrum of the M = 0.40 case, which is believed to be related to the strong circulation and the anti-CRV pair behind the dune shell. The corresponding modes demonstrate the intensive interactions between the coolant and mainstream immediately behind the dune horns. Interestingly, the M = 0.90 case exhibited an exact same frequency (i.e., 15 Hz) as that of the M = 0.40, and the corresponding dynamic mode exhibited an alternative sign behind the dune, which was the result of anti-CRV induction as they traveled along it. Therefore, the shedding frequency of the anti-CRV pair behind the BDSIC was 15 Hz (i.e., St = 0.009) and not a function of the coolant blowing ratio.

4. Conclusions

An experiment was performed to quantify the unsteady adiabatic effectiveness behind the circular hole, the shaped hole (i.e., laidback, fan-shaped hole), and the BDSIC configuration in a low-speed wind tunnel at Shanghai Jiao Tong University. Coated with a fast-response PSP (i.e., 6-kHz dynamic response), the instantaneous effectiveness on the wall surface was resolved successfully with a high-speed camera. Coolant fluid (i.e., CO_2) was discharged from an injection hole at an inclination angle of 35°. The blowing ratio (M) was varied from 0.40 to 1.40. During the experiment, the prominent signature of the flow structure was identified with two-point spatial correlation, and the dominant modes were extracted via DMD analysis.

The coolant film of the circular hole attached well to the surface at a blowing ratio (M) of 0.40 but partially separated from the plate at M = 0.90. Their corresponding SDs indicated significantly enhanced fluctuations near the hole as the film started to separate, which was the result of energetic turbulent structures atop the surface. The signatures of horseshoe vortices and CRV pairs were identified from the large dataset with two-point spatial correlation. Detailed analysis qualitatively showed that these flow structures made the greatest contribution to the effectiveness fluctuations. The dominant oscillating frequencies for a circular hole were determined by DMD analysis to be 45 and 13 Hz (i.e., corresponding to St = 0.026 and 0.008, respectively) at M = 0.40 and 0.90, respectively. While the dynamic mode with St = 0.026 was believed to be related to the sweeping behavior of JICF at M = 0.40, the event

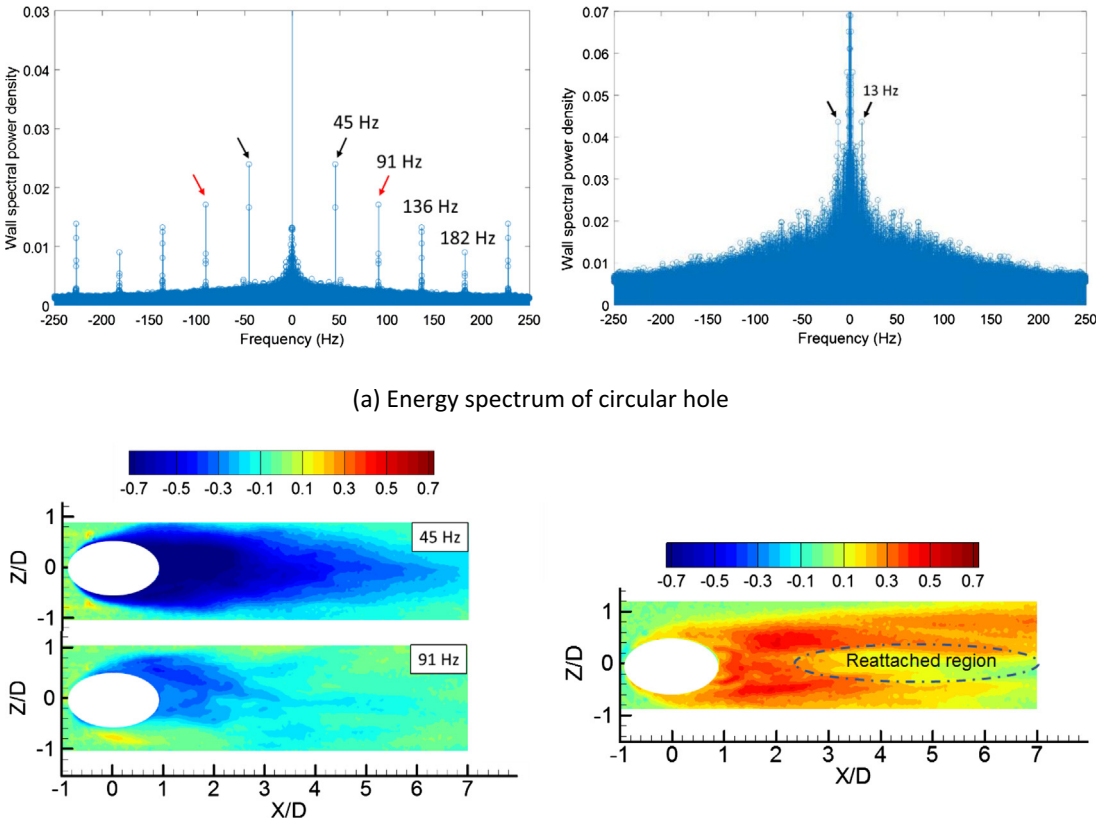

Fig. 12. DMD analysis for the circular hole at blowing ratios of $M = 0.40$ (left) and $M = 0.90$ (right).

with $St = 0.008$ could have been associated with the dynamic reattachment of the coolant jet because it partially separated from the surface at $M = 0.90$.

As for the shaped hole, the measured ensemble-averaged effectiveness showed much better film coverage for the shaped hole than for the circular configuration. No jet separation was observed during the tests. At a blowing ratio (M) of 0.40, increased fluctuation was observed at the exit of the coolant hole due to the insufficient momentum of the coolant jet. When the blowing ratio (M) was increased to 0.90 and 1.40, the high SD regions moved from the hole exit to the lateral side of the hole. Two-point spatial correlations qualitatively revealed that the coherent structures, including the large-scale CRV and horseshoe-like vortices, were responsible for the increasing fluctuations in effectiveness. As for the DMD analysis, no dominant mode was extracted from the measured instantaneous effectiveness.

The measured effectiveness of the test case with BDSIC was found to be significantly higher than that of the circular and shaped holes. With the assistance of a dune shell, it was able to provide much wider film coverage over the protected surface. Except for the regions along the axis of dune horns, the measured SDs were much smaller than those of the other two configurations at $M = 0.90$ and 1.40. Coherent structures of existing circulation flows and anti-CRV pairs were determined clearly by two-point correlation at $M = 0.40$. In addition to the anti-CRV pair, a strong shear was identified behind the BDSIC concept at $M = 0.90$. The DMD analysis extracted a dominant mode with frequency of 15 Hz (i.e., corresponding $St = 0.009$) for both tests, which was believed to be the shedding frequency of anti-CRV pair.

For some cases, such as flow structures away from the surface or flow structures superimposed with others, it may be difficult to extract the actual mode frequency from the effectiveness fields, since the measured effectiveness is a scalar field on the test surface whereas JICF is a three-dimensional behavior. However, the measured scalar effectiveness could provide meaningful insight into the effect of near-wall turbulent structures on the adiabatic effectiveness. After all, the dynamic modes of time sequence effectiveness were contributed by coherent flow structures in JICF. This paper represents the first effort to use fast-response PSP sampling at a high frame rate to quantify the unsteady behavior of adiabatic effectiveness over a flat plate. The identified structures and dynamic modes from two-point correlation and DMD analysis are expected to not only serve as a benchmark for computational fluid dynamics validation studies, but also further our understanding of the inherent physics pertinent to film cooling.

Conflict of interest

The authors declare that they have no conflict of interest in relation to this study.

Acknowledgements

The authors gratefully acknowledge financial support for this study from the National Natural Science Foundation of China (11372189).

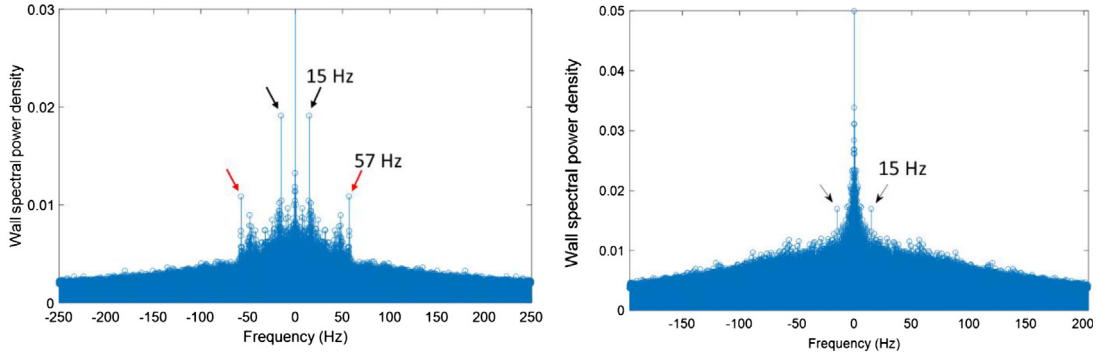

(a) Energy spectrum of BDSIC

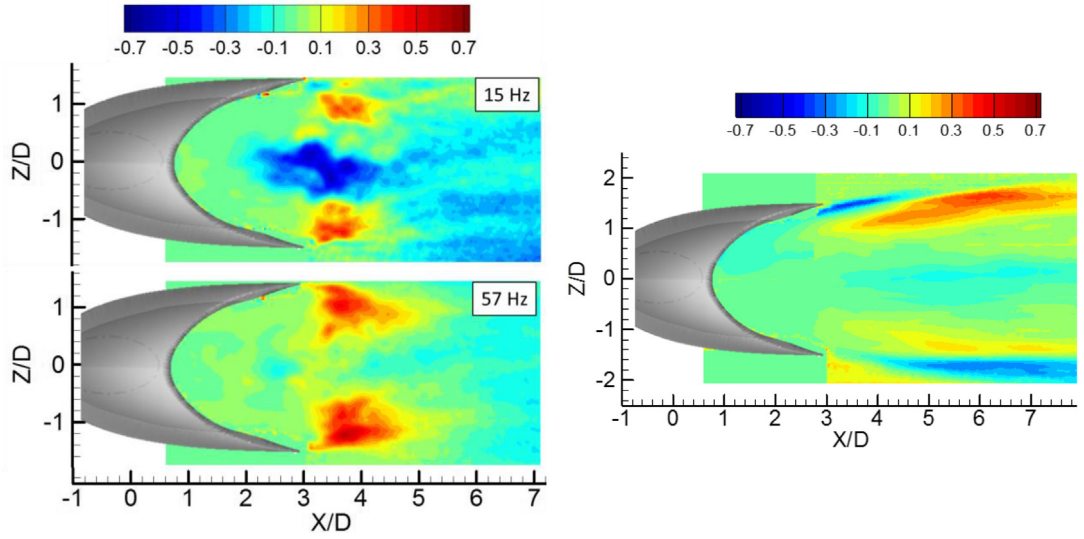

(b) Fluctuation modes (imaginary part only) on cooling surface

Fig. 13. DMD analysis for the BDSIC at blowing ratios of $M = 0.40$ (left) and $M = 0.90$ (right).

Appendix A. Supplementary material

Supplementary data associated with this article can be found, in the online version, at https://doi.org/10.1016/j.ijheatmasstransfer.2018.04.126.

References

[1] D.G. Bogard, K.A. Thole, Gas turbine film cooling, J. Propuls. Power. 22 (2006) 249–270, https://doi.org/10.2514/1.18034.
[2] R.S. Bunker, A review of shaped hole turbine film-cooling technology, J. Heat Transfer 127 (2005) 441, https://doi.org/10.1115/1.1860562.
[3] R.J. Goldstein, E.R.G. Eckert, F. Burggraf, Effects of hole geometry and density on three-dimensional film cooling, Int. J. Heat Mass Transf. 17 (1974) 595–607, https://doi.org/10.1016/0017-9310(74)90007-6.
[4] W. Zhou, B. Johnson, H. Hu, Effects of flow compressibility and density ratio on film cooling performance, J. Propuls. Power 33 (2017) 964–974, https://doi.org/10.2514/1.B36275.
[5] K.-D. Lee, K.-Y. Kim, Shape optimization of a fan-shaped hole to enhance film-cooling effectiveness, Int. J. Heat Mass Transf. 53 (2010) 2996–3005, https://doi.org/10.1016/J.IJHEATMASSTRANSFER.2010.03.032.
[6] W. Zhou, H. Hu, A novel sand-dune-inspired design for improved film cooling performance, Int. J. Heat Mass Transf. 110 (2017) 908–920, https://doi.org/10.1016/j.ijheatmasstransfer.2017.03.091.
[7] R. Schroeder, K. Thole, Adiabatic effectiveness measurements for a baseline shaped film cooling hole, ASME Turbo Expo 2014 (GT2014-25992) (2014) 1–13, https://doi.org/10.1115/GT2014-25992.
[8] T.F. Fric, A. Roshko, Vortical structure in the wake of a transverse jet, J. Fluid Mech. 279 (1994) 1–47, https://doi.org/10.1017/S0022112094003800.
[9] C. Dai, L. Jia, J. Zhang, Z. Shu, J. Mi, On the flow structure of an inclined jet in crossflow at low velocity ratios, Int. J. Heat Fluid Flow 58 (2016) 11–18, https://doi.org/10.1016/j.ijheatfluidflow.2015.12.001.
[10] K. Mahesh, The interaction of jets with crossflow, Annu. Rev. Fluid Mech. 45 (2013) 379–407, https://doi.org/10.1146/annurev-fluid-120710-101115.
[11] G. Bidan, C. Vézier, D.E. Nikitopoulos, Study of unforced and modulated film-cooling jets using proper orthogonal decomposition—part I: unforced jets, J. Turbomach. 135 (2012) 21037, https://doi.org/10.1115/1.4006599.
[12] A.R. Karagozian, The jet in crossflow, Phys. Fluids. 26 (2014) 101303, https://doi.org/10.1063/1.4895900.
[13] P. Kalghatgi, S. Acharya, Modal analysis of inclined film cooling jet flow, J. Turbomach. 136 (2014) 81007, https://doi.org/10.1115/1.4026374.
[14] A. Khojasteh, S. Wang, D. Peng, S. Yavuzkurt, Y.Z. Liu, Structure analysis of adiabatic film cooling effectiveness in the near field of a single inclined jet: measurement using fast-response pressure-sensitive paint, Int. J. Heat Mass Transf. 110 (2017) 629–642, https://doi.org/10.1016/J.IJHEATMASSTRANSFER.2017.03.069.
[15] L.M. Wright, S.T. McClain, M.D. Clemenson, Effect of density ratio on flat plate film cooling with shaped holes using PSP, J. Turbomach. 133 (2011) 41011, https://doi.org/10.1115/1.4002988.
[16] H.D. Ammari, N. Hay, D. Lampard, Simulation of cooling film density ratios in a mass transfer technique, in: Vol. 4 Heat Transf. Electr. Power; Ind. Cogener., ASME, 1989: p. V004T08A025. http://doi.org/10.1115/89-GT-200.
[17] J.N. Shadid, E.R.G. Eckert, The mass transfer analogy to heat transfer in fluids with temperature-dependent properties, J. Turbomach. 113 (1991) 27, https://doi.org/10.1115/1.2927734.
[18] D. Charbonnier, P. Ott, M. Jonsson, F. Cottier, T. Köbke, Experimental and numerical study of the thermal performance of a film cooled turbine platform, in: Asme Turbo Expo 2009, Vol 3, Pts A B, ASME, 2009. http://doi.org/10.1115/GT2009-60306.
[19] B. Johnson, H. Hu, Measurement uncertainty analysis in determining adiabatic film cooling effectiveness by using pressure sensitive paint technique, J. Turbomach. 138 (2016) 121004, https://doi.org/10.1115/1.4033506.

[20] B. Johnson, W. Tian, K. Zhang, H. Hu, An experimental study of density ratio effects on the film cooling injection from discrete holes by using PIV and PSP techniques, Int. J. Heat Mass Transf. 76 (2014) 337–349, https://doi.org/10.1016/j.ijheatmasstransfer.2014.04.028.
[21] D. Peng, C.D. Jensen, T.J. Juliano, J.W. Gregory, J. Crafton, S. Palluconi, T. Liu, Temperature-compensated fast pressure-sensitive paint, AIAA J. 51 (2013) 2420–2431, https://doi.org/10.2514/1.J052318.
[22] D. Peng, S. Wang, Y. Liu, Fast PSP measurements of wall-pressure fluctuation in low-speed flows: improvements using proper orthogonal decomposition, Exp. Fluids. 57 (2016) 45, https://doi.org/10.1007/s00348-016-2130-z.
[23] A.M. Scroggin, E.B. Slamovich, J.W. Crafton, N. Lachendro, J.P. Sullivan, Porous polymer/ceramic composites for luminescence-based temperature and pressure measurement, MRS Proc. 560 (1999) 347, https://doi.org/10.1557/PROC-560-347.
[24] J.W. Gregory, K. Asai, M. Kameda, T. Liu, J.P. Sullivan, A review of pressure-sensitive paint for high-speed and unsteady aerodynamics, Proc. Inst. Mech. Eng. Part G J. Aerosp. Eng. 222 (2008) 249–290, https://doi.org/10.1243/09544100JAERO243.
[25] D.L. Schmidt, B. Sen, D.G. Bogard, Film cooling with compound angle holes: adiabatic effectiveness, J. Turbomach. 118 (1996) 807, https://doi.org/10.1115/1.2840938.
[26] A.K. Sinha, D.G. Bogard, M.E. Crawford, Film-cooling effectiveness downstream of a single row of holes with variable density ratio, J. Turbomach. 113 (1991) 442, https://doi.org/10.1115/1.2927894.
[27] D.R.D. Pedersen, E.R.G. Eckert, R.J. Goldstein, Film cooling with large density differences between the mainstream and the secondary fluid measured by the heat-mass transfer analogy, J. Heat Transfer 99 (1977) 620–627, https://doi.org/10.1115/1.3450752.
[28] J. Han, S. Dutta, S. Ekkad, Gas turbine heat transfer and cooling technology, second ed., CRC Press, New York, 2012.
[29] E. Sakai, T. Takahashi, H. Watanabe, Large-eddy simulation of an inclined round jet issuing into a crossflow, Int. J. Heat Mass Transf. 69 (2014) 300–311, https://doi.org/10.1016/j.ijheatmasstransfer.2013.10.027.
[30] W. Zhou, H. Hu, Improvements of film cooling effectiveness by using Barchan dune shaped ramps, Int. J. Heat Mass Transf. 103 (2016) 442–456, https://doi.org/10.1016/j.ijheatmasstransfer.2016.07.066.
[31] S. Nikolaos, Large Eddy Simulation of the Film Cooling Flow System of Turbine Blades: Public Shaped Holes, INSTITUT SUPERIEUR DE L'AERONAUTIQUE ET DE L'ESPACE, 2016. http://cerfacs.fr/wp-content/uploads/2016/09/CFD_SIMIRIOTIS_STAGE.pdf (accessed November 18, 2017).
[32] P.J. Schmid, Dynamic mode decomposition of numerical and experimental data, J. Fluid Mech. 656 (2010) 5–28, https://doi.org/10.1017/S0022112010001217.
[33] P.J. Schmid, Application of the dynamic mode decomposition to experimental data, Exp. Fluids. 50 (2011) 1123–1130, https://doi.org/10.1007/s00348-010-0911-3.